Journal of Applied Fluid Mechanics, Vol. 15, No. 6, pp. 1851-1867, 2022.
Available online at www.jafmonline.net, ISSN 1735-3572, EISSN 1735-3645.
https://doi.org/10.47176/jafm.15.06.1185

Unsteady Fluid Flow Analysis of Tongue Geometry in a Centrifugal Pump at Design and Off-design Conditions

M. Mahdi†, M. Rasekh and V. Sajadi

Energy Conversion Department, School of Mechanical Engineering, Shahid Rajaee Teacher Training University, Tehran, Tehran, 1678815811, Iran

†*Corresponding Author Email: m.mahdi@sru.ac.ir*

(Received March 16, 2022; accepted June 14, 2022)

ABSTRACT

In the present work, the effects of modifying the tongue geometry of a centrifugal pump on pressure pulsations under the design and off-design conditions are carried out numerically by the unsteady analysis of fluid flow. Numerical modeling based on the Re-Normalization Group (RNG) k-ε turbulence model using a Mosaic mesh structure, a technology which can easily, quickly and formally connects any type of mesh for complex geometries and flow regimes, is applied to simulate the flow within the modeled pump, which is validated with the available experimental results. The flow is simulated through a commercial Computational Fluid Dynamics (CFD) software that solved Reynolds-Averaged Navier-Stokes (RANS) equations for a three-dimensional unsteady flow. In addition to choosing Q_d (the design flow rate), $0.4Q_d$ and $1.2Q_d$ are also taken into account as the inlet flow rates. Besides, pressures of $101KPa$ and $13KPa$ are considered as additional inlet conditions for this investigation. This unsteady simulation employing different inlet conditions is used to investigate the impacts of various volute tongue angles on the pressure coefficient (c_p). Results indicate that, overall, by changing the angle from 40° to 85°, the value of the pressure coefficient at the pump outlet grows by about 10% where it also causes a rise in the amplitude of pressure fluctuations. By the same token, a decrement to the inlet flow rate up to 40% of the nominal value brings about the amplitude of pressure fluctuations at the pump outlet to be increased significantly.

Keywords: Unsteady flow simulation; Centrifugal pump model; Off-design conditions; Computational Fluid Dynamics (CFD); Pressure fluctuations.

NOMENCLATURE

b	impeller blade thickness at leading edge	P_{in}	pump shaft power input
b_2	impeller outlet width	Q	pump volumetric flow rate
b_3	volute casing outlet width	Q_d	Pump design flow rate
c_p	pressure coefficient	RANS	Reynolds-Averaged Navier-Stokes
d_h	impeller hub diameter	RET	Richardson Extrapolation Technique
D_1	impeller inlet diameter	RNG	Re-Normalization Group
D_2	impeller outlet diameter	RSI	Rotor-Stator Interaction
D_3	volute casing base circle diameter	t	time step
e_a	approximate relative error	T	an impeller rotation time period
e_{ext}	extrapolated relative error	u_2	impeller exit peripheral velocity
GCI	Grid Convergence Index	u_i	flow time-averaged velocity
GGI	General Grid Interface	α	flow incidence angle
H	pump head	β_1	impeller blade inlet angle
H_d	pump design head	β_{1flow}	impeller blade inlet flow angle
n	impeller rotating speed	β_2	impeller blade outlet angle
n_s	pump specific speed	η	pump efficiency
N	number of mesh cells	μ	absolute viscosity
NPSH	Net Positive Suction Head	μ_t	turbulent viscosity
$NPSH_3$	NPSH at 3% loss in total head	ρ	density
p	pump static pressure	φ_{ext}	extrapolated value
p_{ref}	pump inlet (reference) pressure	ϕ	angular spacing
P	apparent order	ψ	head coefficient

1. INTRODUCTION

Centrifugal pumps are used in the majority of all fluid flow processes. The complexities of the fluid flow patterns and design practicalities for these pumps have involved intensive engineering endeavors for well over 100 years (Adams 2017).

The flow in both stationary and rotating internal flow passages of centrifugal pumps is quite complicated. Even when operating at the best efficiency point 100% design flow, centrifugal pump internal flow fields are somewhat unsteady. At off-design operating flows, the internal flows are highly unsteady (Adams 2017).

The flow at the impeller outlet is non-uniform. The diffuser vanes or volute cutwaters are thus approached by an unsteady flow. The flow in the stator acts back on the velocity field in the impeller. The related phenomena are called "rotor/stator interaction" (RSI). As a consequence of the RSI, hydraulic excitation forces are generated. These give rise to pressure pulsations, mechanical vibrations, and alternating stresses in various pump components. The pressure pulsations excite the pump casing to vibrations. They travel as fluid-borne noise through the piping system, generating vibrations of the pipe walls. The vibrating walls and structures radiate air-borne noise (Gülich 2020).

Among the various pump geometrical parameters, such as inlet, impeller, volute casing (circular wall), tongue shape in the casing, and cross-sectional area of throttle (a valve to regulate the flow); volute casing and tongue play a significant role in performance control in off-design conditions. This critical role shows that a correct choice of parameters related to the tongue area (for instance, the volute tongue angle) is necessary for the best design of the volute casing (Lorett and Gopalakrishnan 1986). Related experimental and numerical studies carried out for analyzing centrifugal pumps instability and fluid flow are as follows:

Dong *et al.* (1997) studied the effect of modifications to tongue and impeller geometries on the flow structure and resulting noise in a centrifugal pump. They found that a significant reduction of noise is achieved by increasing the gap between the tongue and the impeller up to about 20 percent of the impeller radius.

Li (2004) mapped the unsteady flows in the volute of a single-stage, cantilevered centrifugal pump at both best efficiency and part-loading points. Results showed that the more closely the measuring point approaches the volute tongue, the larger the fluctuations in velocity and flow angle become.

Al-badawi *et al.* (2018) investigated the influence of four types of blade angle on a very low specific speed centrifugal pump, and throughout their numerical results found out that the blade with the smallest length decreases the pump head and benefits from the best velocity distribution.

Zhang *et al.* (2019) investigated the effects of modifying the blade pressure side on unsteady pressure pulsations and flow structures in a low specific speed centrifugal pump by experimental and numerical methods. It was observed that the pressure amplitudes were attenuated evidently at major measuring positions, specifically at high flow rates.

Mahdi *et al.* (2020) inquired about the effects of the tongue geometry on the cavitation and performance of a centrifugal pump in off-design conditions. Their three-dimensional numerical research showed that the higher tongue angles caused an improvement in the head and efficiency of the pump, especially in high flow rates.

Lu *et al.* (2020) studied the influences of volute tongue angle on hydraulic performance and fluid stability. The results showed that the pressure pulsation intensity near the volute tongue is larger. In addition, with the increase of the volute tongue angle, the hydraulic efficiency under large flow conditions is improved.

Zhang *et al.* (2020) researched the effect of the volute tongue cut on pressure pulsations of a low specific speed centrifugal pump using three volute tongues. In this study, they revealed that cutting the volute tongue will lead to the pressure energy increasing.

Shim and Kim (2020) investigated the flow instability and its correlations with performance characteristics for a centrifugal pump. Obtained results detected three different types of flow instability in partial-load conditions: inside the volute, upstream of the impeller, and at the interface between the impeller and the volute.

Lv *et al.* (2021) studied the internal flow stability in a high specific speed centrifugal pump at partial load. Their numerical work revealed that the backflow at the volute tongue is the chief factor of the caused instability, which grows with the decrease of the flow rate.

Li *et al.* (2021) redesigned a double-suction centrifugal pump to reduce the reported noise and vibration. This intention which was done by adding to impeller blades as well as increasing the radial gap between the impeller and volute, resulted in about 6% of decrease in pressure fluctuation amplitudes.

Wu *et al.* (2021b) analyzed the dynamic instability of a double-blade centrifugal pump via extracting time and frequency domains at 16 crucial points. They noted that high vorticity magnitude occurs in the vicinities of the blade trailing edge and tongue of the volute due to the RSI between the impeller and the volute.

Wu *et al.* (2021a) carried out the effects of modifying the blade pressure side on unsteady pressure pulsation and flow structures in a low specific speed centrifugal pump. They concluded that the reduction of pressure pulsation attributes to unloading the pressure side of the modified blades.

Cui *et al.* (2021) introduced the vortex identification method to clarify the internal correlation between unsteady flow structures with pressure pulsations. They illustrated that the RSI between a relatively big

trailing vortex core and volute tongue generates larger pressure pulsation and radial force in the pump at a low flow rate.

Lin *et al*. (2021a) investigated four types of volute tongue in order to reduce the vibration noise and energy loss within a centrifugal pump. The results of their study showed that sinusoidal tubercle volute tongues are able to minimize the pressure pulsations by about 15% while increasing the pump efficiency up to around 1%.

Yang *et al*. (2021) studied the inter-stage variability of pressure pulsation inside an electrical submersible pump. Results indicate that when the number of stages is high, the pressure pulsations caused by the interference phenomenon can seriously threaten the operational stability by inducing vibration and noise.

Lin *et al*. (2021b) researched the impact of impeller sinusoidal tubercle trailing edge on pressure pulsations of a centrifugal pump and learned that it can offer a decrease in pressure pulsations by about 45% at the pump discharge and up to around 30% at the volute throat.

Zhu *et al*. (2022) studied five different incident angles for the wear-ring clearance of a centrifugal pump and showed that the improved efflux angle, not only weaken the impact disturbance of the leakage flow but also improve the pump efficiency, flow losses and vibration amplitude.

It is understood from recent research that the emphasis on analyzing pressure pulsations in the unsteady flow of a centrifugal pump is still of the priorities of researchers. Although, to the best of authors' knowledge, modifying a volute tongue geometry in an unsteady fluid flow concerning pressure fluctuations under the design and off-design conditions to investigate instabilities in whole parts of a centrifugal pump including discharge nozzle, volute casing, impeller vane passage, and volute tongue sides, has not been studied yet. Besides, all of the papers as mentioned earlier did their numerical procedures using traditional mesh generation techniques, which are time-taking yet somewhat low precision methods, specifically in unsteady 3D simulations.

The present study numerically analyzes the unsteady flow in a centrifugal pump with a volute using the Reynolds-Averaged Navier-Stokes (RANS) equations to investigate instabilities throughout the pump and tries to modify them by changing the angle of the volute tongue. As a novel technique, this paper benefits from the Mosaic mesh method to speed up the simulation procedure and enhance the quality and precision of the unsteady 3D run. It is worth mentioning that not only the design flow rate but also various off-design flow rates are applied as inputs to enrich the content of the paper.

The article is organized as: in the previous section, a study on the importance of centrifugal pumps and flow unsteadiness phenomena resulting in pump vibrations has been introduced. In the following section, the problem statement, including the pump model, design parameters, simulation software, and approaches besides grid independence and temporal resolution, is investigated. Afterward, pressure fluctuations as flow instabilities in various nodal points inside the centrifugal pump are plotted as figures after the simulated pump model is validated by available experimental measurements. At last, a conclusion is drawn from this research.

2. PROBLEM FORMULATION

2.1 Centrifugal Pump Model

The single-stage centrifugal pump considered in this work consists of a shrouded impeller with six backswept blades, a straight suction pipe, and a spiral volute casing with a circular-shaped cross-section, as shown in Figure 1. The impeller inlet diameter D_1 is 65 *mm* with an outlet diameter D_2 of 165 *mm* and an outlet width b_2 of 7 *mm*. The impeller blade thickness at the leading edge *b* is 0.7 *mm* with blade inlet angle β_1 of 28°, blade outlet angle β_2 of 30°, and impeller hub diameter d_h of 40 *mm.* Also, the incidence angle α, which is equal to the difference between inlet blade angle β_1 and inlet flow angle β_{1flow}, is 14° (Figure 2). The flow from the impeller is discharged into a spiral volute casing with a base circle diameter D_3 of 176 *mm* and volute outlet width b_3 of 20 *mm*. The impeller is designed to operate at 2900 *rpm* with the specific speed n_s of 66 based on

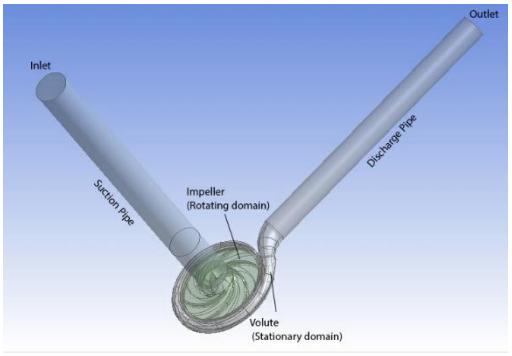

Fig. 1. Computational Domain.

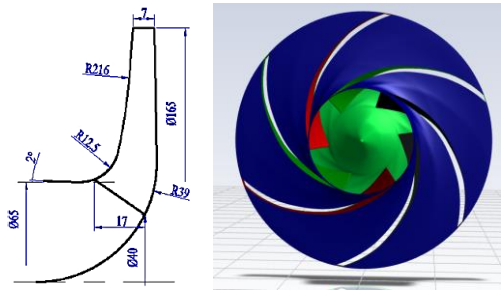

(a) **(b)**

Fig. 2. 2D views of a) the impeller blade (Fu *et al.* 2015), and b) the whole impeller.

Table 1. Design parameters of the modeled centrifugal pump

Parameter	Value
D_1	65 *mm*
D_2	165 *mm*
b_2	7 *mm*
b	0.7 *mm*
β_1	28°
β_2	30°
d_h	40 *mm*
α	14°
β_{1flow}	-
D_3	176 *mm*
b_3	20 *mm*
n	2900 *rpm*
n_s	66
H_d	32 *m*
Q_d	25 m^3/h
$NPSH_3$	1.6 *m*

the formula ($3.65\left(n\sqrt{Q}/H^{3/4}\right)$). The specified pump design head H_d and design flow rate Q_d are 32 m and 25 m^3/h, respectively, with its net positive suction head representing a 3% loss in the total head due to cavitation $NPSH_3$ of 1.6 m. The detailed specifications of the corresponding centrifugal pump are tabulated in Table 1.

2.2 Numerical Methods

The commercial Computational Fluid Dynamics (CFD) code ANSYS Fluent-2020 R2 has been used for investigating the internal flow of the pump numerically. The flow solver of the code is applied for the incompressible turbulent flow and the continuity equation besides the three-dimensional time-averaged Navier-Stokes equations. Furthermore, the numerical solutions are acquired based upon a conservative, fully-implicit, and element-based finite volume method in discretizing the conservation equations for mass and momentum.

$$\frac{\partial u_i}{\partial x_i} = 0 \tag{1}$$

$$\rho\left[\frac{\partial u_i}{\partial t} + \frac{\partial u_i u_j}{\partial x_j}\right] = \frac{\partial}{\partial x_j}\left[(\mu + \mu_t)\frac{\partial}{\partial x_j}\right] - \frac{\partial p}{\partial x_i} \tag{2}$$

where u_i , ρ , μ , μ_t and p are, respectively, the component of time-averaged velocity, density, absolute and turbulent dynamic viscosities, and static pressure. The first equation, also called the continuity equation, states that the incoming and outgoing mass flows are identical in magnitude for a given control volume under steady conditions while the latter, which is derived from the Newton's second law of mechanics, indicates that the change of the momentum of a mass over time is equal to the vectorial sum of all volume and surface forces acting on the mass (Gülich 2020). A high-resolution scheme presented by Barth and Jesperson (1989) is utilized to discretize the advection terms in space besides a second-order backward Euler scheme in time for the transient term. In addition, a number of inner iterations are fulfilled in each time step for the unsteady analysis. Kindly note that, the CFD code manual (ANSYS 2019) has clarified all these numerical strategies in detail (Shim and Kim 2020).

The Re-Normalization Group (RNG) k-ε model (Orszag and Yakhot 1986) with a scalable wall function is used as the turbulence model. Although the RNG k-ε model is reasonably simple, it could export precise results compared to the standard one as the flow near the wall is solved with more details. Furthermore, the strength of this model mainly happens when the recirculation flow occurs in the internal impeller cross-flow of centrifugal pumps, turbines, and fans (Adanta *et al*. 2018).

As Figure 1 depicts the computational domain, it is composed of all the passages of the volute, impeller, suction pipe and also, discharge pipe. Lengths of suction and discharge pipes are, respectively, 5 and 10 times the impeller inlet diameter. These, not only allow the flow recirculation upstream of the impeller and the separation downstream of the volute to be resolved, but also dismiss the ideal boundary conditions from impeller and other important parts of the pump. For simplifying the simulation, side chambers and wear-ring clearance have been neglected.

The working fluid is water at 25 ℃ besides considering the reference pressure of 1 atm. For boundary conditions, the total pressure is prescribed at the domain inlet, and mass flow rate is set at the domain outlet according to the working conditions. Also, the no-slip condition is imposed at solid walls, and the General Grid Interface (GGI) model is utilized to connect stationary and rotary domains. The frozen rotor interface model is used for the steady simulation to treat the flow from one component to the next by changing the reference frame. Furthermore, the transient rotor-stator interface model is applied into the unsteady simulation, which considers all the transient flow characteristics and allows a smooth rotation between components (Zhu *et al*. 2012).

2.3 Mosaic Mesh

Introducing Mosaic from ANSYS, an evolution in CFD simulations that hold forth solutions that optimize the mesh everywhere while do not compromise accuracy for speed. Mosaic mesh which is a Fluent Meshing technology accelerates the meshing process with a reduced face count, higher quality cells and efficient parallel scalability. Thanks to Mosaic-enabled poly-Hexcore meshing, engineers have been able to not only decrease the number of meshing cells by 15% but also reaching solution times that are often twice as fast; 45% faster while requiring 30% less memory, as the ANSYS company has officially announced (Zore *et al*. 2020).

Indeed, transitioning between varying types of mesh elements in complex geometries and flow regimes has long been a major simulation challenge in the industry. Mosaic technology meets this challenge by automatically connecting different types of meshes with general polyhedral elements. Poly-Hexcore, the first application of Mosaic technology, fills the bulk

region with octree hexes, maintains a high-quality layered poly-prism mesh in the boundary layer and conformally unites these two meshes with general polyhedral elements.

Poly-Hexcore meshing formally can easily and quickly connect any type of mesh for complex geometries and flow regimes. Allowing to explore more materials, variations and possibilities, this technology offers simplicity and authenticity (Zore *et al*. 2019).

Figure 3 shows the grid distribution for the simulated pump. A Mosaic mesh type is applied in all parts of the pump, including the impeller, the volute, and the suction and discharge pipes using the ANSYS Fluent Meshing 2020 R2 software. Besides, all the layers near the volute solid surface are exposed to an expansion ratio of 1.2 to resolve the high-velocity gradient caused by the boundary layer. The first grid points from the solid surfaces are placed in the log-law region at $y^+ < 1$ to ensure the accuracy of the results.

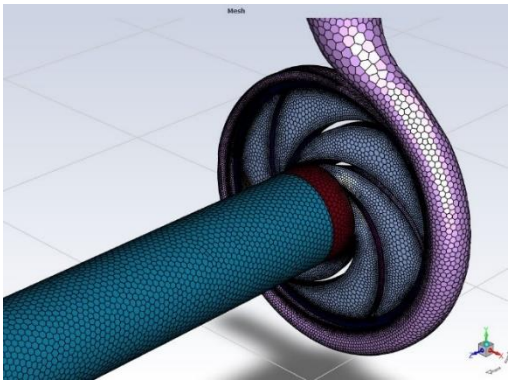

(a)

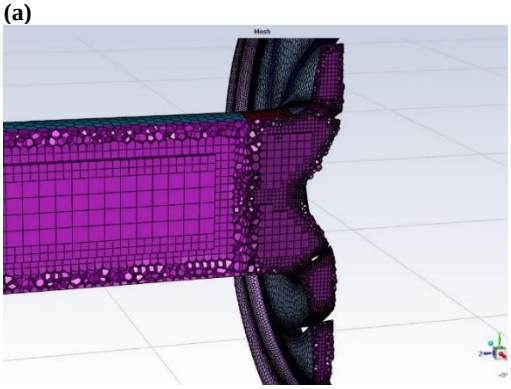

(b)

Fig. 3. Grid distribution of the computational domain; a) the whole pump model, b) a cross-section of the model.

Figure 4 illustrates the different nodal points employed to investigate the unsteady pressure fluctuations in the pump model. The monitoring nodal points are selected in the volute casing, the discharge nozzle, and on both sides of an impeller, blade as well as both sides of the tongue to make sure that all of the sections are covered for the instability analysis (Majidi 2005). The nodal points DM1, DM2, and DM3 (D stands for Discharge nozzle and M for Midspan) are located in the beginning, middle, and end of the pump discharge nozzle, respectively. In addition, the points VM1, VM2, VM3, and VM4 (V stands for Volute casing and M for Midspan) are located, respectively, in the volute casing having a relative angular spacing of 90 degrees, measured from the volute tongue ($\phi = 0$). Moreover, points TM1 and TM2 (T stands for Tongue side and M for Midspan) are located directly on the volute tongue at the impeller and discharge nozzle sides, respectively. Eventually, the nodal points SM1, SM2, PM1, and PM2 (S stands for Suction side, P for Pressure side and M for Midspan) are located at the inlet and outlet of an impeller blade by which 1SM and 2SM are located at the suction side, and 1PM and 2PM at the pressure side of the blade. Kindly note that all these points are located at the mid-span plane of the pump model.

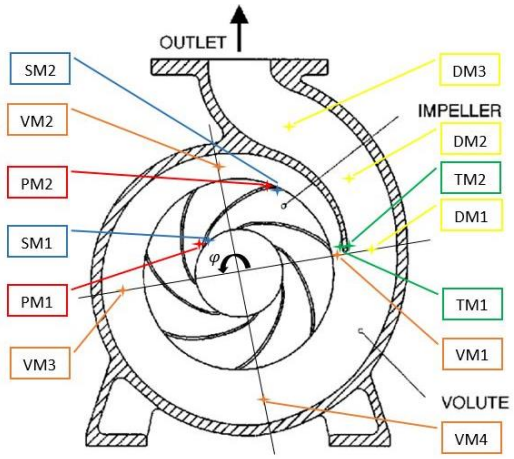

Fig. 4. Monitoring locations for unsteady pressure fluctuations.

The results of a steady RANS simulation serve as the initial flow fields of the unsteady RANS (URANS) analysis to facilitate the convergence. The convergence criteria for the governing equations and mass imbalance at each time-step are set to root-mean-square residuals below 10^{-5} and 0.005%, respectively, while the coefficient loops number per iteration is set to 10. The simulation procedure is done using a 3.10 GHz Intel(R) E5507 Quad-Core Processor (Core i7), benefiting from 32 GB of RAM running on a 64 bit Windows 10. This makes it possible for a URANS simulation to be completed in about 24 hours.

2.4 Grid Independence and Temporal Resolution

The Grid Convergence Index (GCI) criterion is employed to discover the grid-independent results. For this purpose, the Richardson Extrapolation Technique (RET) explained by Celik and Karatekin (1997) is exerted to improve the grid resolution. As demonstrated in Table 2, values of the head coefficient (ψ) (a dimensionless coefficient characterizes the head generated by a pump under certain operating conditions and assumed to be constant for pumps with similar flow conditions (Wilson *et al*. 2006)) at the design flow rate (Q_d) in

Table 2. Grid-independent results in different mesh grids

Parameter	Value
N1/ N2/ N3	601,235/ 1,412,440/ 3,874,161
r	1.3
ψ_1	0.1363
ψ_2	0.1345
ψ_3	0.1341
P	1.6
φ_{ext}^{21}	0.1347
$e_a^{21}(\%)$	0. 347
$e_{ext}^{21}(\%)$	0.124
$GCI_{fine}^{21}(\%)$	0.15

a steady state simulation are obtained for three types of computational grids (coarser, medium, and finer). In this table, P is actually the apparent order of the method, and φ_{ext} is the extrapolated numerical solution (Celik and Zhang 1995). Due to the grid refinement factor, which is set to 1.3, the number of cells in the medium grid in three dimensions is about 2.2 times more than the coarser grid. According to the obtained results, the ψ values represent a uniform convergence from coarser to finer mesh grids, besides, the values of GCI and the extrapolated relative error for the medium grid type are, respectively, 0.15% and 0.124%. Therefore, for the next simulations, the medium grid type using 1,412,440 mesh elements, which its details in each domain are described in Table 3, is chosen.

Table 3. Details of mesh cells in subdomains

Domain	Type of meshes	Number of mesh cells	Averaged y^+
Suction pipe	Mosaic	226,376	51.2
Impeller	Mosaic	705,241	97.9
Volute and Discharge pipe	Mosaic	480,823	104.5

In the transient simulation, the time step size of 3.45×10^{-4} seconds regarding 3 degrees of revolution per time step is selected. In order to make a balance between the numerical accuracy and computational cost, the time histories of ψ at Q_d for different time steps regarding 1, 2, 3, and 6 degrees of revolutions in each time step are obtained and then compared to one another. According to these results, plotted in Figure 5, the average value of ψ using 6 degrees of revolution is 1.072, while the other three have no significant differences in average. As a 1-degree case requires more than three times as much time as a 3-degree case to perform the calculations, the unsteady simulations in this paper are done using a 3-degree revolution. By considering the mentioned time step size corresponding to the chosen revolution, the maximum courant number and the root-mean-square values are, respectively, around 90 and 8.

The head coefficient (ψ) is a characteristic coefficient, derived from the corresponding physical quantity according to the affinity laws and used to characterize the operating behavior. This dimensionless parameter which is assumed to be

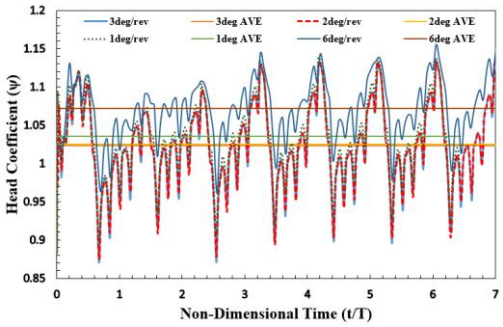

Fig. 5. Time histories of ψ at Q_d for different time steps.

constant for pumps with similar flow conditions is calculated regarding the following equation in which H is the pump head, and u_2 is the peripheral velocity at the impeller exit (Ye *et al.* 2020).

$$\psi = \frac{H}{u_2^2/2g} \tag{3}$$

2.5 Validation

In this section, present numerical results are compared with the available experimental data obtained by Fu *et al.* (2015) to validate the modeled pump. In this regard, the head (H) and efficiency (η) of the pump, as two of the most important parameters used for examining the accuracy of simulated centrifugal pumps, are utilized. The following equation has been employed to calculate the pump efficiency which is equal to the power of the water produced by the pump divided by the pump's shaft power input (Ye *et al.* 2020).

$$\eta = \frac{\rho g H Q}{P_{in}} \tag{4}$$

where ρ, Q, and P_{in} are, respectively, the working fluid density, volumetric flow rate, and power input to the pump shaft. Performance curves of the centrifugal pump model illustrated in Figures 6 and 7 compare the present numerical results to the available experimental data (Fu *et al.* 2015). Results of Figure 6, a graph of pump head (H) in a range of flow rates (Q), slightly underestimate the pump head compared to the experimental data. The slope of the experimental head curve is gentle at flow rates lower than 25 m^3/h and becomes a little steeper at higher ones, which the trend is predicted reasonably well by the present numerical results. The existed deviation between the two lines is less than 5% and therefore negligible regarding the assumptions made throughout the simulation. The reason for the computational head to be less than the experimental one could be the precision of the simulated modeled pump geometry, or the physical features of the simulated working fluid, not completely being fit with the actual conditions. It must also be pointed out that the difference between the experimental and numerical curves becomes greater at flow rates higher than 30 m^3/h. In Figure 7, a graph of pump efficiency (η) over the former range of flow rates (Q), overall, the efficiency is somehow overpredicted by numerical results compared to the

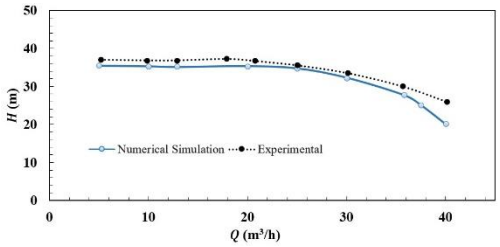

Fig. 6. Comparing the numerical simulation pump head with the experimental one.

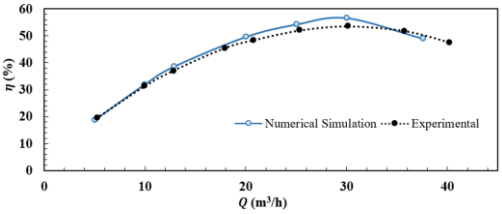

Fig. 7. Comparing the numerical simulation pump efficiency with the experimental one.

corresponding experimental data, yet; the trend is estimated well, again. To justify this overestimation, by referring to Equation (4) to calculate the pump efficiency, the power input is located at the denominator of the fraction. The input power is also proportional to the torque required to rotate the pump impeller. The only difference between numerical and experimental input power may be the losses that exist in the experimental mode and are not calculated in the numerical mode. In other words, the experimental input power is expected to be higher than the numerical one, and therefore the experimental efficiency is lower. Apart from the mentioned justifications, Probable sources of errors in these two figures could be friction loss by leakage flow from the seals and disk friction loss, of which they have noticeable effects on shaft power (Shim and Kim 2020).

3. RESULTS AND DISCUSSION

In the present section, the unsteadiness and flow instabilities inside the discharge nozzle, the volute casing, the impeller vane passage, and of the tongue insides are investigated at design and off-design conditions in different volute tongue profiles and reference pressures. For this purpose, the pressure distributions in nodal points of each part are measured using the unsteady simulations at various flow rates, inlet pressures, and tongue angles. The pressure distributions are illustrated in a normalized form to let the scaling of pressure pulsation data concerning the size and speed. Thus, the pressure coefficient (c_p), which is a non-dimensional parameter, is employed to measure the value of pressure fluctuations in an entire revolution period as follows (Si *et al.* 2014).

$$c_p = \frac{p - p_{ref}}{0.5\rho u_2^2} \tag{5}$$

Indeed, the pressure coefficient which describes the relative pressures throughout a flow field is the ratio of pressure forces to inertial forces. In the aforementioned equation, p is the pressure at the desired point, and p_{ref} is the inlet pressure with values of 101325 Pa and 13000 Pa, which are considered as the reference pressures. Kindly note that, the former pressure value is the standard atmospheric pressure while the latter is chosen since it brings about the modeled pump to form relatively small and thin cavities, specifically developing on the blade suction sides (Fu *et al.* 2015). Also, the impeller outlet tip velocity (peripheral velocity at the impeller exit) u_2 equals 20 m/s according to the rotational speed of 2900 rpm. Each impeller rotation (entire revolution period) T requires 318 time steps t, and each time step is about 20.69 milliseconds, equivalent to 1.13 degrees of impeller rotation. As the base tongue angle of the modeled IS65-50-160 type centrifugal pump is 62.5° (Fu *et al.* 2015), an amount of $\pm 22.5°$ higher and lower of the base angle are supposed to investigate the effects of the volute tongue angle on pressure pulsations and flow instabilities in various parts. In this regard, three types of tongue angles of 40° (Tongue B), 62.5° (Tongue A), and 85° (Tongue C) are considered while the tongue thickness is a constant value of 1 millimeter. Indeed, as it is illustrated in Figure 8, this study aims to analyze the effects of repositioning the volute cutwater by cutting it back from tongue B to tongue A, and from tongue A to tongue C which will result in an increase in the volute throat area. Summary of the analyzed parameters is given in Table 4. Kindly note that to prevent the multiplicity of the figures, obtained curves of pressure pulsations under 120% of the flow rate are presented, applying only the base tongue angle, i.e., 62.5°. For the other two angles, the results are similar, and the trends of the curves are the same.

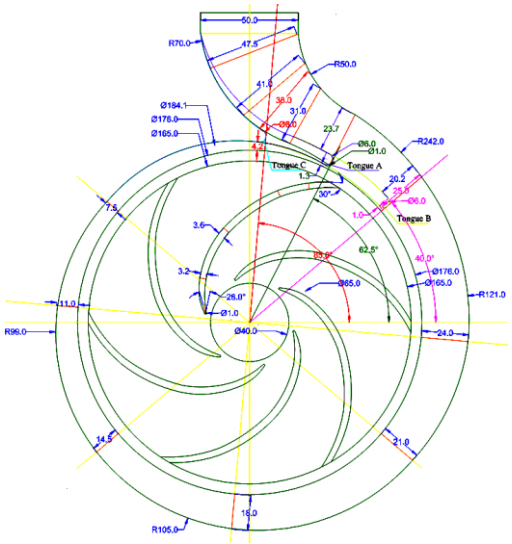

Fig. 8. A detailed sketch of the modeled pump including the three tongue types.

Flow instabilities throughout the discharge nozzle from DM1 to outlet nodal points at 101325 Pa inlet pressure and flow rates of Q_d and 0.4 Q_d are depicted in Figures 9 and 10, respectively. Also, for

Table 4. Values of analyzed parameters

Parameter	Values
Volute tongue angle	40° ,62.5°, 85°
Volute tongue thickness	1 mm
Pump inlet flow rate	$0.4Q_d$, Q_d, $1.2Q_d$
Pump inlet pressure	101325 Pa, 13000 Pa

describing these fluctuations at a reference pressure of 13000 Pa while using the same flow rates, Figures 11 and 12 are drawn, respectively. To better understand the effects of off-design conditions on pressure pulsations of the discharge nozzle, fluctuations of c_p at the flow rate of 1.2 Q_d are shown in Figure 13.

3.1 Flow Instability inside the Discharge Nozzle

According to Figure 9, as the position of the volute angle increases at the design flow rate condition, the pressure coefficient also increases at each nodal point, while the pressure difference between nodes of DM2 and DM3 decreases with the outlet point. In addition, the amplitude of pressure fluctuations at the DM1 node is reduced.

In an off-design condition, about 40% of the nominal flow rate in Figure 10, the pressure fluctuations of the four points DM1, DM2, DM3, and Outlet are significantly matched. In this case, as the position of the tongue angle increases from 40° to 62.5°, pressure coefficient values and fluctuations remain nearly unchanged, while in the case of 62.5° to 85°, the amounts, and oscillations of this coefficient decrease at any point. In addition, the oscillations amplitude of c_p in 85° of the tongue angle is more regular than the other two positions during the impeller's period, especially at the beginning of the rotation.

As the inlet pressure decreases at the design flow rate, in Figure 11, the pressure fluctuations also decrease, but general characteristics of the diagrams are the same as the standard pressure mode under design flow rate. In these diagrams, also, the mode of oscillation reduction continues with the completion of the impeller rotation.

Besides, the decrease of inlet pressure in the case of lower volumetric flow rate is shown in Figure 12, which has the same characteristics as the standard pressure of lower flow rate case, although, in the angular position of 85°, mean pressure fluctuations have increased.

As the flow rate increases to about 120% of the design flow rate in Figure 13, the average values of the pressure coefficient decrease, yet the fluctuations are totally the same as the decreased inlet pressure mode of the design flow rate diagrams, even more regular than that. As the inlet pressure reduces, the oscillation curve is accompanied by a discontinuity with a very high oscillation amplitude, which indicates the formation of cavitation bubbles at the nozzle outlet and strongly influences the pressure pulsations.

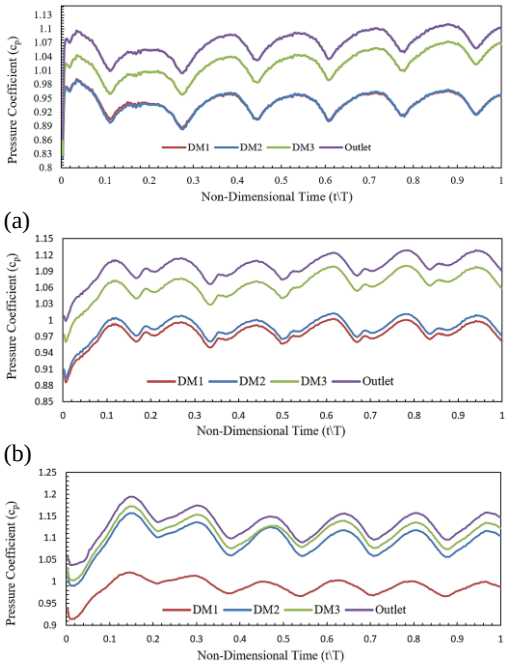

Fig. 9. Unsteady pressure fluctuations in the discharge nozzle nodal points at the inlet pressure of 101325 Pa under the design flow rate using tongue angular positions of a) 40°, b) 62.5°, and c) 85°.

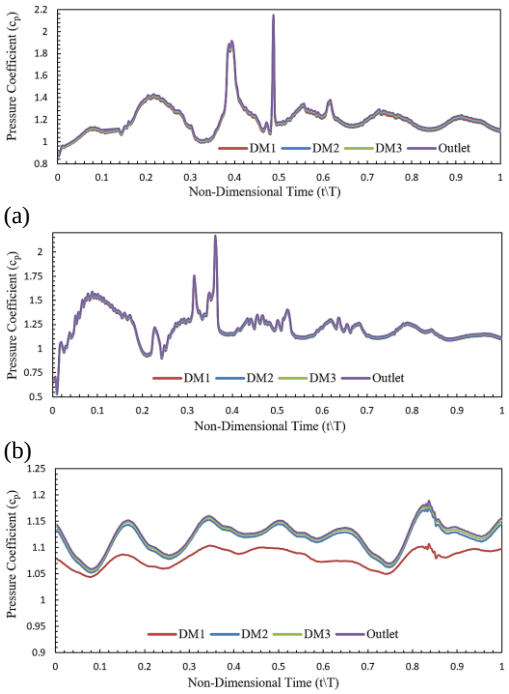

Fig. 10. Unsteady pressure fluctuations in the discharge nozzle nodal points at the inlet pressure of 101325 Pa under 40% of the design flow rate using tongue angular positions of a) 40°, b) 62.5°, and c) 85°.

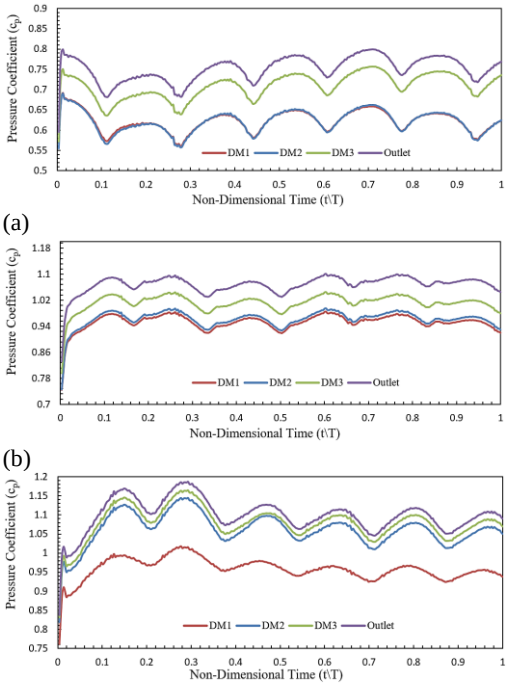

Fig. 11. Unsteady pressure fluctuations in the discharge nozzle nodal points at the inlet pressure of 13000 Pa under the design flow rate using tongue angular positions of a) 40°, b) 62.5°, and c) 85°.

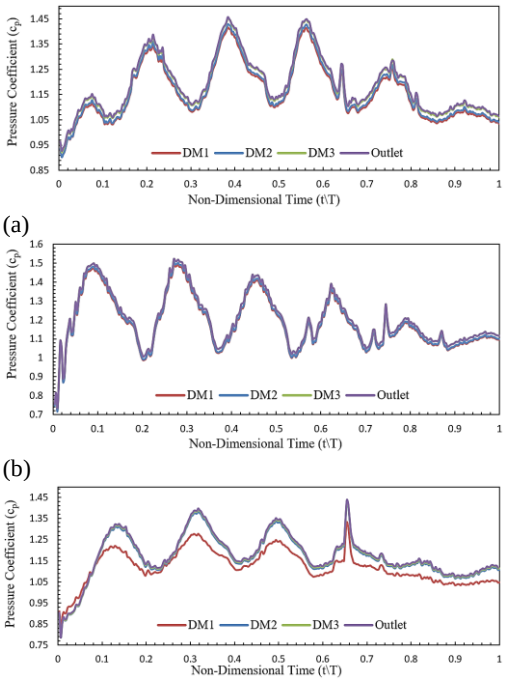

Fig. 12. Unsteady pressure fluctuations in the discharge nozzle nodal points at the inlet pressure of 13000 Pa under 40% of the design flow rate using tongue angular positions of a) 40°, b) 62.5°, and c) 85°.

3.2 Instability inside the Volute Casing

Figure 14 shows the variations of the pressure

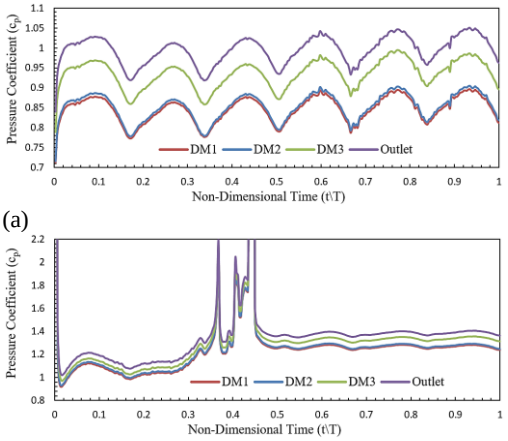

Fig. 13. Unsteady pressure fluctuations in the discharge nozzle nodal points under 120% of the design flow rate using tongue angular position of 62.5° at inlet pressures of a)101325 Pa and b) 13000 Pa.

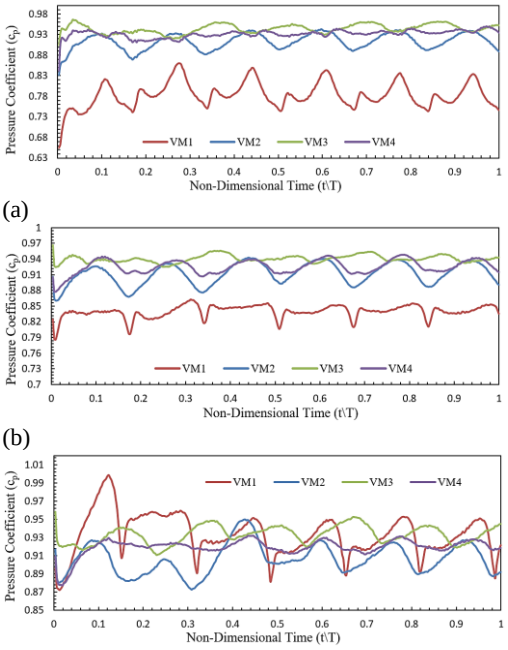

Fig. 14. Unsteady pressure fluctuations in the volute casing nodal points at the inlet pressure of 101325 Pa under the design flow rate using tongue angular positions of a) 40°, b) 62.5°, and c) 85°.

coefficient at VM1, VM2, VM3, and VM4 with time for different angular positions of the volute tongue applying 101325 Pa of reference pressure at Q_d flow rate. According to Figure 14(a), VM1 nodal point, which is closer to the tongue, has less pressure than the other nodal points, but its oscillation amplitude is greater. According to Figures 14(b) and 14(c), with increasing the tongue angle, the pressure differences of the points decrease; in other words, the pressure related to VM1 increases, and its average becomes closer to the rest. Overall, as the angular position increases, the amplitude of the oscillations also raises, and they lose their general order.

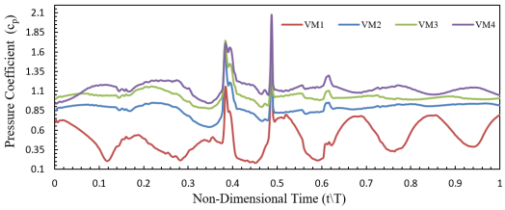

(a)

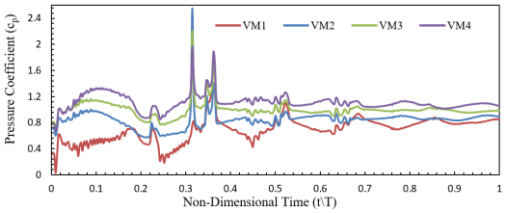

(b)

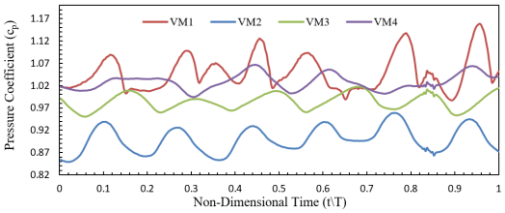

(c)

Fig. 15. Unsteady pressure fluctuations in the volute casing nodal points at the inlet pressure of 101325 Pa under 40% of the design flow rate using tongue angular positions of a) 40°, b) 62.5°, and c) 85°.

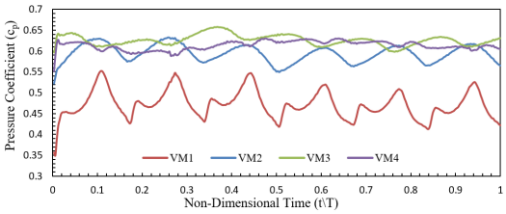

(a)

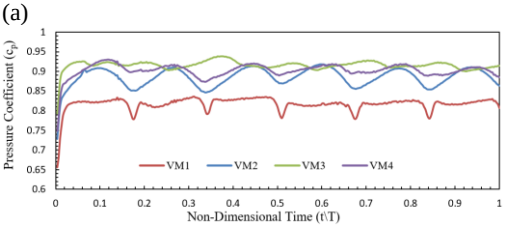

(b)

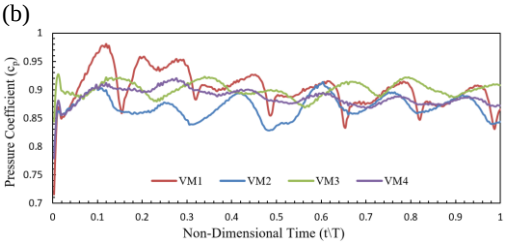

(c)

Fig. 16. Unsteady pressure fluctuations in the volute casing nodal points at the inlet pressure of 13000 Pa under the design flow rate using tongue angular positions of a) 40°, b) 62.5°, and c) 85°.

Furthermore, the nodal point VM3 has the highest average pressure coefficient in the states of 40 and 62.5 degrees, while, these conditions occur to VM4 in Figure 15 where the flow rate decreases to $0.4Q_d$.

Figure 15 shows the pressure coefficient changes of these points for an off-design condition where the inlet flow rate is 40% of the nominal value. In this case, the general characteristics of the diagrams are similar to the nominal mode, and with increasing the angular position, the amount of VM1 pressure increases so that it has higher pressure at an angle of 85 degrees than the rest of the points. Decreasing the flow rate increases the pressure coefficient of all points and also increases the amplitude of pressure fluctuations compared to the nominal state.

According to Figure 16, the inlet pressure of 13000 Pa under the flow rate of Q_d has a significant impact on lowering the amplitude of c_p compared to the inlet pressure of 101325 Pa. Furthermore, as the tongue angle changes from 40° to 62.5° and then 85°, the amplitude of pressure pulsations lessens, and along with that, the average value of c_p grows. This growth becomes more severe, especially in VM1 nodal point.

Changes in the pressure coefficient of different points within the pump volute due to the pressure of 13000 Pa and the flow of 40% of the nominal flow are shown in Figure 17. In this case, the trend of pressure coefficient changes is similar to Figure 15, and the values of the pressure coefficient are nearly the same as the previous mode at each point. Specifically, by decreasing the inlet pressure, pressure fluctuations in Figure 17 also decrease, but the general features of these diagrams are the same as the standard pressure modes. Besides, by following Figures 17(a) to 17(c), the curve of the point VM1 approaches the curve of the point VM4, like in Figures 15 and 16, which demonstrates as the tongue angle increases, it is expected to see small pressure difference throughout the volute casing regardless of various inlet pressures and flow rates.

For the inlet pressures of 101325 Pa and 13000 Pa at the tongue angle of 62.5°, the pressure coefficient alters within the volute nodal points at a 1.2 Q_d flow rate, which is shown in Figure 18. According to Figure 18(a), for the inlet pressure of 101325 Pa, variations in c_p are uniform and change in the range of 0.73 to 0.93. Besides, by increasing the flow rate to 1.2 Q_d in Figure 18(a), the average value of c_p decreases, and in particular, this decreasing is more tangible in point VM4 as its curve, compared to Figure 14(b), approaches VM1 curve. As the inlet pressure of the oscillation curves decreases, a discontinuity in Figure 18(b) is associated with a very high oscillation amplitude and, as interpreted in Figure 13, indicates the formation of cavitation bubbles, which strongly influences the pressure fluctuations.

3.3 Instability inside the Impeller Vane Passage

Unsteady pressure distributions in an entire revolution period of the impeller at nodal points PM2 and SM2 inside one of the vane passages are shown in Figures 19 to 23. According to Figure 19, with

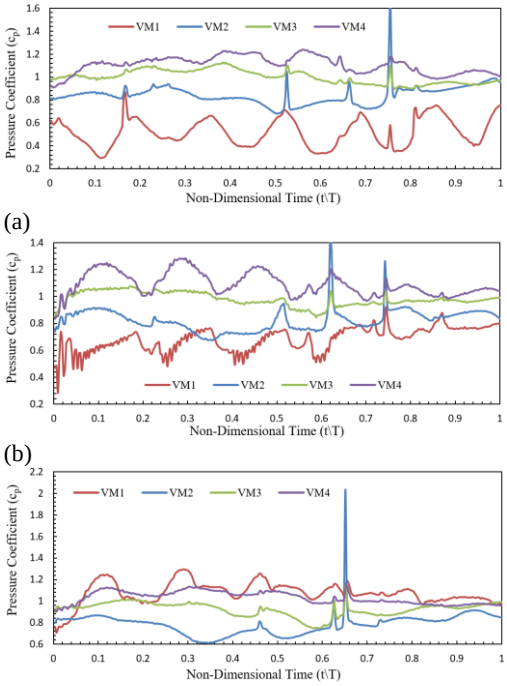

Fig. 17. Unsteady pressure fluctuations in the volute casing nodal points at the inlet pressure of 13000 Pa under 40% of the design flow rate using tongue angular positions of a) 40°, b) 62.5°, and c) 85°.

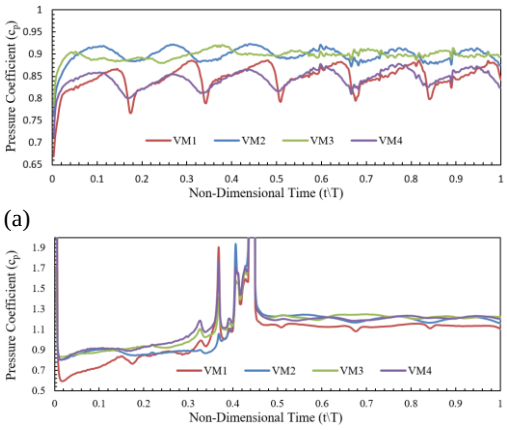

Fig. 18. Unsteady pressure fluctuations in the volute casing nodal points under 120% of the design flow rate using tongue angular position of 62.5° at inlet pressures of a)101325 Pa and b) 13000 Pa.

increasing the angular position of the tongue geometry, the average value of c_p at SM2 nodal point also increases, while the average value of this parameter for the PM2 point decreases with increasing tongue angle from 40 to 62.5 degrees. Again, by increasing this angle to 85° for the point PM2, the pressure coefficient mean value raises and reaches its maximum value among the mentioned cases. Also, by referring to the obtained diagrams, it could be understood that in both 40 and 85 degrees, the effect of the tongue angle on the pressure fluctuations on both sides of the tongue is more significant. At the same time, in these two cases, PM2 and SM2 show similar oscillating behaviors. Also, by comparing diagrams 19(a), 19(b), and 19(c), it is clear that the angular position of 85° has the highest oscillation amplitudes.

In an off-design condition of 0.4 Q_d (represented in Figure 20), the PM2 curve at the angular position of 62.5° has the lowest value of the pressure coefficient between the cases and also compared to SM2 curves. The negative values of c_p, in this case, refer to pressure values less than the reference pressure considered in the eye of the impeller.

In addition, generally, with decreasing the inlet pressure, pressure coefficient mean values and ranges of fluctuations in Figures 21 and 22 are dropped, but wholescale characteristics of the graphs are the same as the standard pressure graphs. However, a detailed examination reveals that at 40° of the tongue angle, with decreasing the pressure, only the average value of c_p decreases, and there is little change in its oscillation amplitude (Figure 21(a)). Also, at 62.5° in Figure 21(b), there is not much change in the amplitude and mean value of c_p. By increasing the angle to 85°, as shown in Figure 21(c), although the average value of the pressure coefficient increases, the amplitude of the oscillations decreases somewhat. With reducing the flow rate at 13000 Pa reference pressure in 40 degrees of angular position, although the average pressure coefficient did not change much, the amplitude of oscillations became smaller in Figure 22(a) compared to Figure 20(a). The most crucial point is the complete elimination of the sudden pulse, created in $t/T = 0.5$ in Figure 20 (a). Furthermore, in Figure 22(b), for both PM2 and SM2 nodal points, the amplitude and mean value of c_p are reduced, besides a significant note that sudden pulses in the curves of these two points created in Figure 20(b) is completely eliminated in Figure 22(b). Figure 22(c) does not show much change in amplitude and the average value of c_p compared to the standard pressure mode in Figure 20(c).

By growing the volumetric flow rate to $1.2Q_d$, depicted in Figure 23(a), for the SM2 nodal point, although the mean value of c_p decreases, the amplitude of the oscillations increases. A very interesting point in this figure occurred in the PM2 curve, where, although the amplitude of the fluctuations did not change much, the amount of c_p increases sharply, which causes the PM2 curve to be placed above the SM2 curve, unlike the previous cases. As the inlet pressure in Figure 23(b) decreases, the curves of these two points change their places again.

Kindly note that, PM1 and SM1, located at the impeller eye, are of minor significance for this study as variations in the tongue angle could barely affect the pressure fluctuations in this point. An important issue for these two nodal points, as was referred by Majidi (2005), is existence of negative pressure coefficient indicating a pressure lower than the reference point around this region.

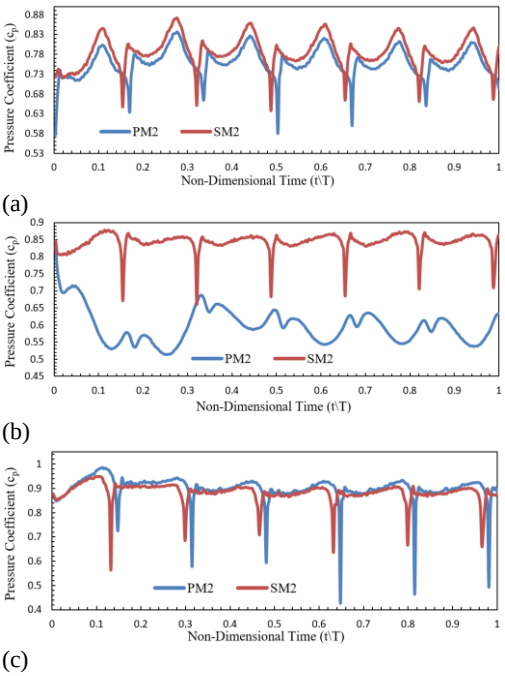

Fig. 19. Unsteady pressure fluctuations in the impeller vane passage nodal points at the inlet pressure of 101325 *Pa* under the design flow rate using tongue angular positions of a) 40°, b) 62.5°, and c) 85°.

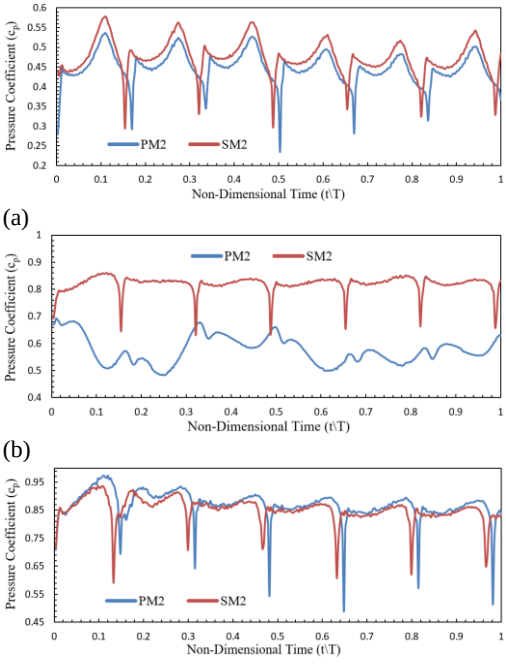

Fig. 21. Unsteady pressure fluctuations in the impeller vane passage nodal points at the inlet pressure of 13000 *Pa* under the design flow rate using tongue angular positions of a) 40°, b) 62.5°, and c) 85°.

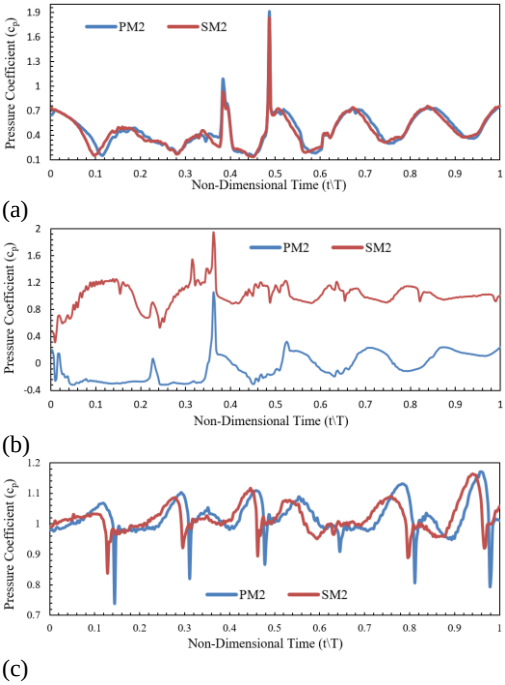

Fig. 20. Unsteady pressure fluctuations in the impeller vane passage nodal points at the inlet pressure of 101325 *Pa* under 40% of the design flow rate using tongue angular positions of a) 40°, b) 62.5°, and c) 85°.

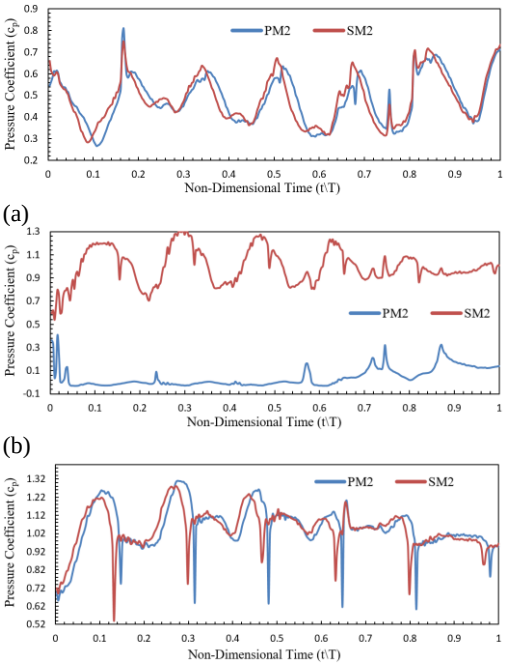

Fig. 22. Unsteady pressure fluctuations in the impeller vane passage nodal points at the inlet pressure of 13000 *Pa* under 40% of the design flow rate using tongue angular positions of a) 40°, b) 62.5°, and c) 85°.

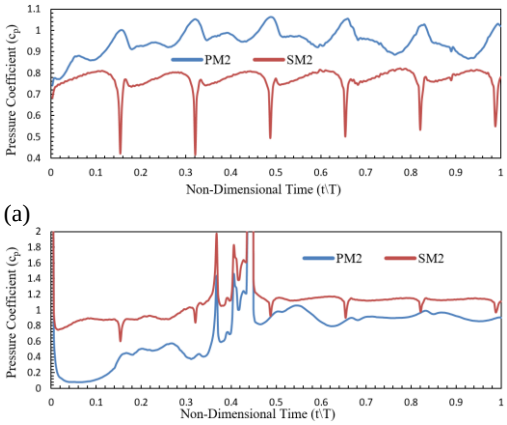

Fig. 23. Unsteady pressure fluctuations in the impeller vane passage nodal points under 120% of the design flow rate using tongue angular position of 62.5° at inlet pressures of a)101325 *Pa* and b) 13000 *Pa*.

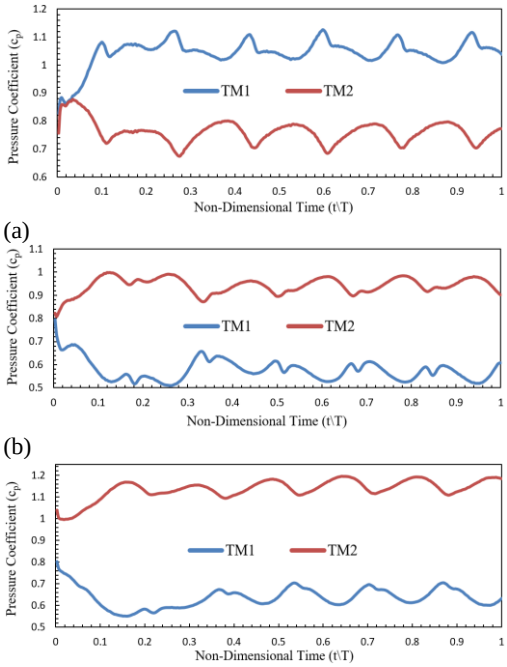

Fig. 24. Unsteady pressure fluctuations of tongue sides nodal points at the inlet pressure of 101325 *Pa* under the design flow rate using tongue angular positions of a) 40°, b) 62.5°, and c) 85°.

3.4 Instability of Tongue Sides

In this section, unsteady pressure distributions on both sides of the pump cutwater at two points, TM1 on the impeller side and TM2 on the outlet side, are shown in Figures 24 to 28.

According to Figure 24(a), at a pump angular position of 40 degrees, the pressure coefficient on the tongue impeller side is higher than the outlet side, which reaches its maximum value when the blade arrives at the tongue and has the lowest value just moments before the blade reaches the tongue. Also, whenever the TM1 nodal point has the highest value of pressure coefficient, TM2 takes the lowest value. This behavior of cutwater, which involves the intense interaction of pressure fluctuations on both sides, multiplies its importance in the volute casing. In addition, the passage of the impeller blades creates an alternating velocity and pressure field in the vicinity of the volute tongue. This unsteady flow field is prone to cavitation creation and has different effects on various cavitation phenomena in the tongue. For example, it is well known that unstable cavitation is the most erosive type of cavitation (Dular *et al*. 2004), thus, it is not surprising that sometimes the local erosion damage of the centrifugal pump cutwater is found after being under an overload condition for long periods of time (Brennen 1994). Another point is that the amplitude of fluctuations in TM1 and TM2 curves is exactly the same at any moment. As the angular position increases, TM1 and TM2 curves are replaced with each other, while general characteristics of 40° are preserved. The reason for the replacement of point TM1 with TM2 in two positions of 62.5 and 85 degrees is due to the reduction of incident angle of the outlet fluid from the impeller trailing edge with the cutwater. Increasing the angular position, in addition to reducing the angle of incidence, also increases the pressure difference between the two sides of the tongue. This can be clearly seen in Figure 24. It is noteworthy that as the angular position of the volute tongue increases, the amplitude of the pressure coefficient oscillations for both TM1 and TM2 remains almost unchanged. The magnitude of this coefficient also increases for TM2 nodal point with increasing the tongue angle, while for TM2 point, this value decreases sharply with increasing the angle from 40° to 62.5° and grows slightly again with increasing this angle from 62.5° to 85°.

By diminishing the flow rate to 40% of the nominal flow rate in Figure 25, compared to the diagrams in Figure 24 at the nominal flow rate, the pressure fluctuations curve of the nodal point TM1 has changed place with TM2 curve in 40° of the angular position and maintains this position in the other two tongue angles in continue, nevertheless, the difference in pressure coefficient between the two sides of the tongue has increased. At point TM2, with increasing the angular position, especially to 85 degrees, the amplitude of the oscillations is drastically reduced, while in these diagrams, the oscillation is damped with more rotation of the impeller. The negative values of c_p at this point refer to the pressure coefficients less than the reference pressure, which is considered in the eye of the impeller.

By diminishing the inlet pressure to *13000* Pa, it can be seen from Figure 26 that under the design flow rate of Q_d, the average values of c_p drop somewhat in 40°, on both sides of the tongue. Moreover, comparing three types of tongue angles depicts that the higher the angle, the lower the pressure coefficient in TM1, while the opposite of this statement stands for TM2.

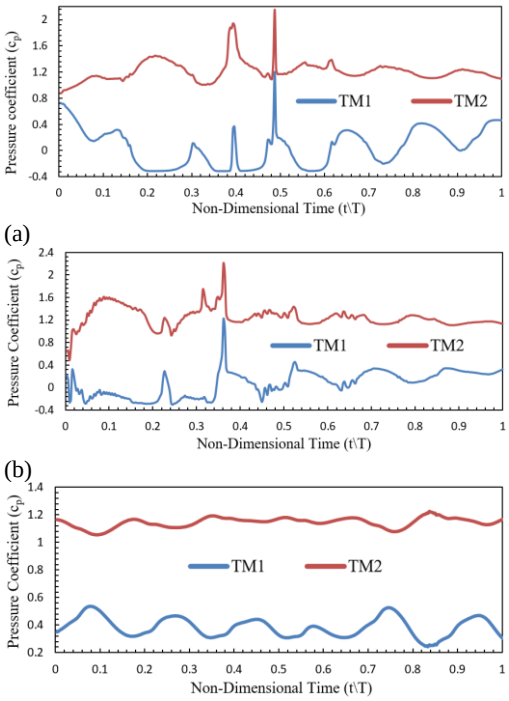

Fig. 25. Unsteady pressure fluctuations of tongue sides nodal points at the inlet pressure of 101325 *Pa* under 40% of the design flow rate using tongue angular positions of a) 40°, b) 62.5°, and c) 85°.

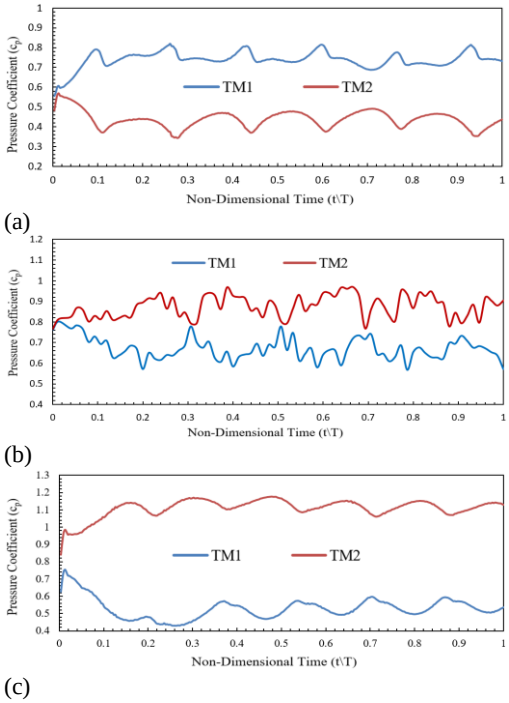

Fig. 26. Unsteady pressure fluctuations of tongue sides nodal points at the inlet pressure of 13000 *Pa* under the design flow rate using tongue angular positions of a) 40°, b) 62.5°, and c) 85°.

This decrease in inlet pressure at a lower flow rate is shown in Figure 27, which in this case has the same standard pressure characteristics at 40% of the design flow rate, except that the sudden fluctuations created at angles of 40 and 62.5 degrees have been eliminated. Also, this time the pressure fluctuations in TM1 at an angle of 85 degrees have a mean value of about zero, which indicates equality with the inlet pressure at this point. Also, in these curves in Figure 27, the amplitude of pressure oscillations at point TM2 tends to the zero value.

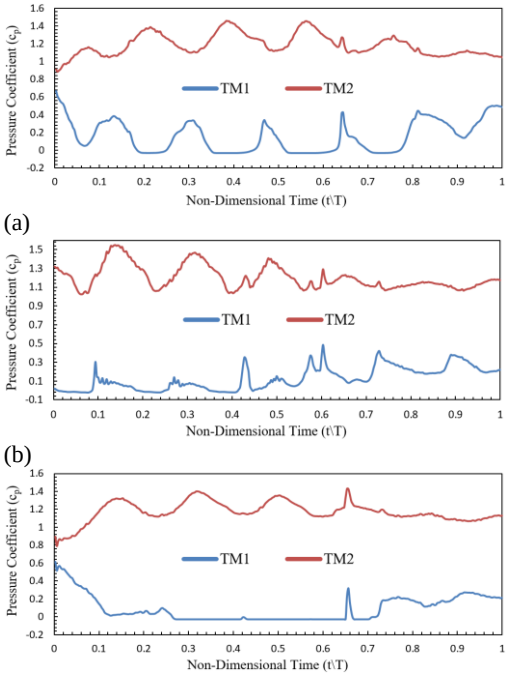

Fig. 27. Unsteady pressure fluctuations of tongue sides nodal points at the inlet pressure of 13000 *Pa* under 40% of the design flow rate using tongue angular positions of a) 40°, b) 62.5°, and c) 85°.

Under the flow rate of 1.2 Q_d in Figure 28, it can be noticed that decreasing the inlet pressure drops the average value of c_p around TM1 while increases this value about TM2. Another interesting happening is doubling the amplitude of c_p in TM2 while becoming approximately constant in TM1.

4. CONCLUSION

In this paper, by numerically solving the Reynolds-Averaged Navier-Stokes (RANS) equations, the flow inside the pump is transiently simulated. First, the results obtained in the steady state were compared with the experimental results, which had acceptable accuracy. Next, simulations were performed for different angular positions of the pump volute tongue in different operating conditions, and the distribution of pressure coefficient at different nodal points of the pump were presented in graphs over time. In general, by changing the angle from 40° to 85°, the value of the pressure coefficient at the pump outlet increases by about 10%; this is not a surprising outcome as the increase in the volute cutwater angle (repositioning

the volute cutwater by cutting it back) will bring about a raise in the volute throat area (Figure 8), which makes c_p to go up when focusing on the same volumetric flow. Moreover, by this volute cutwater raise, the amplitude of pressure fluctuations also see a rise. In addition, by reducing the inlet volume flow rate to 40% of the nominal value, the amplitude of pressure fluctuations at the pump outlet rises significantly.

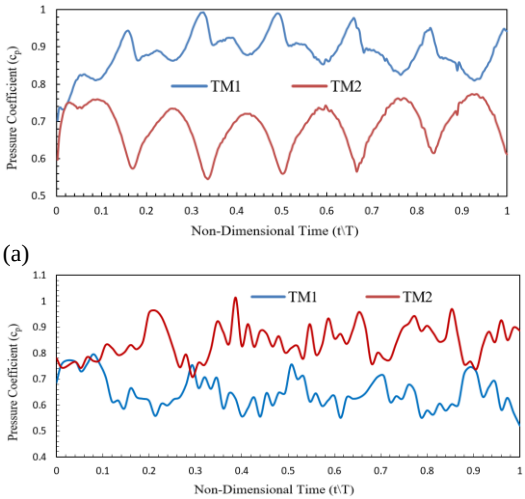

(a)

(b)

Fig. 28. Unsteady pressure fluctuations of tongue sides nodal points under 120% of the design flow rate using tongue angular position of $62.5°$ at inlet pressures of a)$101325\ Pa$ and b) $13000\ Pa$.

The position of the tongue also affects the pressure distribution within the volute. Increasing the tongue angle reduces the pressure variations along the tongue length, but at each nodal point of the volute casing, the amplitude of the fluctuations grows. The tongue's position has a significant effect on the pressure coefficient around the tongue, especially in off-design conditions, and the possibility of cavitation in this area is higher than in other parts of the pump since stronger strikes are observed in this region. The following detailed results from this research is also of great importance:

1- As the position of the volute angle increases at the design flow rate condition, the pressure coefficient also increases, overall. However, this augmentation is not much severe at 62.5°, and in some nodal points, it is a declining trend.

2- By utilizing the tongue angle of 85° in the off-design condition of $0.4Q_d$, sudden detrimental pulsations within various regions of the pump are smoothened considerably, which could be of great importance for practical usages.

3- At design flow rate condition and under *13kPa* of inlet pressure, the increment in the angle of the volute tongue results in an overall growth in the average value of pressure fluctuations in various parts of a centrifugal pump.

4- Selecting an 85° tongue angle at the off-design condition of $0.4Q_d$ under the inlet pressure of *13kPa*, could smoothen the flow instabilities in most parts of a centrifugal pump, yet it would generate seldom but severe pulses specifically inside impeller vane passages and inside the volute casing near the suction passage.

5- At the off-design condition of $1.2Q_d$, by reducing the inlet pressure, the oscillations are accompanied by a discontinuity which might be a sign of the formation of cavitation bubbles and could correspondingly stimulates the flow unsteadiness in most regions of the pump.

It must be noted that regarding the results of the previous studies, it could be figured out that the aforementioned results and conclusions in the current study are still stood by changing the structural parameters of the pump model, i.e., utilizing another centrifugal volute pump type. Indeed, although the trends of the curves could be similar to the ones of this research, the values of pressure pulsations and the amplitudes might change slightly. A generalization to the achieved outcomes of this research could be made in future works. In addition, investigating the frequency domain over time could be another possible potential for future studies of this research to fully comprehend the instabilities inside the pump model.

REFERENCES

Adams, M. L. (2017). *Power Plant Centrifugal Pumps: Problem Analysis and Troubleshooting*, CRC Press.

Adanta, D., B. Budiarso and A. I. Siswantara (2018). 'Assessment of turbulence modelling for numerical simulations into pico hydro turbine', *Journal of Advanced Research in Fluid Mechanics and Thermal Sciences* 46, 21-31.

Al-badawi, M., I. G. Adam, S. Haddara and A. H. El Sherif (2018), November. Influence of Blade Shape Geometry on Very Low Specific Speed Centrifugal Pump Performance. In *ASME International Mechanical Engineering Congress and Exposition* (Vol. 52101, p. V007T09A075). American Society of Mechanical Engineers.

ANSYS (2019). *ANSYS CFX-Solver Theory Guide-Release 19.0*, ANSYS, Canonsburg, PA.

Barth, T. and D. Jespersen (1989). The design and application of upwind schemes on unstructured meshes. In *27th Aerospace sciences meeting*, 366.

Brennen, C. E. (1994) *Hydrodynamics of pumps*, Concepts ETI and Oxford Science Publications.

Celik, I. and O. Karatekin (1997). Numerical experiments on application of Richardson extrapolation with nonuniform grids. *Journal of Fluids Engineering* 119(3), 584-590.

Celik, I. and W. M. Zhang (1995). Calculation of numerical uncertainty using Richardson

extrapolation: application to some simple turbulent flow calculations. *Journal of Fluids Engineering* 117(3), 439-445.

Cui, B., Y. Zhang and Y. Huang (2021). Analysis of the pressure pulsation and vibration in a low-specific-speed centrifugal pump, *Journal of Fluids Engineering* 143(2), 021201.

Dong, R., S. Chu and J. Katz (1997). Effect of modification to tongue and impeller geometry on unsteady flow, pressure fluctuations, and noise in a centrifugal pump, *Journal of Turbomachery* 119(3), 506-515.

Dular, M., B. Bachert, B. Stoffel and B. Širok (2004). Relationship between cavitation structures and cavitation damage 257, 1176-84.

Fu, Y., J. Yuan, S. Yuan, G. Pace, L. d'Agostino, P. Huang and X. Li (2015). Numerical and experimental analysis of flow phenomena in a centrifugal pump operating under low flow rates, *Journal of Fluids Engineering* 137, 011102.

Gülich, J. F. (2020). *Centrifugal Pumps*. Springer International Publishing.

Li, Q., S. Li, P. Wu, B. Huang and D. Wu (2021). Investigation on reduction of pressure fluctuation for a double-suction centrifugal pump, *Chinese Journal of Mechanical Engineering* 34, 1-18.

Li, W. G. (2004). Effect of volute tongue on unsteady flow in a centrifugal pump', *International Journal of Turbo & Jet-Engines* 21, 223-32.

Lin, P. F., P. F. Song, Z. C. Zhu and X. J. Li (2021a). 'Research on the rotor-stator interaction of centrifugal pump based on sinusoidal tubercle volute tongue. *Journal of Applied Fluid Mechanics* 14(2), 589-600.

Lin, Y., X. Li, B. Li, X. Jia and Z. Zhu (2021b). Influence of impeller sinusoidal tubercle trailing-edge on pressure pulsation in a centrifugal pump at nominal flow rate. *Journal of Fluids Engineering* 143(9) 091205.

Lorett, J. A. and S. Gopalakrishnan (1986). Interaction between impeller and volute of pumps at off-design conditions, *Journal of Fluids Engineering* 108, 12-18.

Lu, R., J. Yuan, L. Wang, Y. Fu, F. Hong and W. Wang (2020). Effect of volute tongue angle on the performance and flow unsteadiness of an automotive electronic cooling pump, *Proceedings of the Institution of Mechanical Engineers, Part A: Journal of Power and Energy*, 0957650920915306.

Lv, J., W. Xu, H. Yin, Y. Zhang and H. S. Dou (2021). Numerical Simulation of the Internal Flow Stability in a Centrifugal Pump with High Specific Speed at Partial Load, *Iranian Journal of Science and Technology, Transactions of Mechanical Engineering*, 1-16.

Mahdi, M., V. Sajjadi and M. Rasekh (2020). Numerical Study of the tongue geometry effects on the cavitation and performance of a centrifugal pump in off-design conditions, *Iranian Journal of Mechanical Engineering Transactions of the ISME* 21, 87-109.

Majidi, K. (2005). Numerical study of unsteady flow in a centrifugal pump, *Journal of Turbomachinary* 127, 363-71.

Orszag, S. A. and V. Yakhot (1986). Renormalization group analysis of turbulence. In *Proceedings of the International Congress of Mathematicians*, 1395-99.

Shim, H. S. and K. Y. Kim (2020). Relationship Between Flow Instability and Performance of a Centrifugal Pump With a Volute, *Journal of Fluids Engineering* 142(11), 111208.

Si, Q., J. Yuan, S. Yuan, W. Wang, L. Zhu and G. Bois (2014). Numerical investigation of pressure fluctuation in centrifugal pump volute based on SAS model and experimental validation, *Advances in Mechanical Engineering* 6, 972081.

Wilson, K. C., G. R. Addie, A. Sellgren and R. Clift (2006). *Centrifugal Pumps* (pp. 190-226). Springer US.

Wu, C., W. Zhang, P. Wu, J. Yi, H. Ye, B. Huang and D. Wu (2021a). Effects of blade pressure side modification on unsteady pressure pulsation and flow structures in a centrifugal pump, *Journal of Fluids Engineering* 143(11), 111208.

Wu, D., S. Yao, R. Lin, Y. Ren, P. Zhou, Y. Gu and J. Mou (2021b). Dynamic Instability Analysis of a Double-Blade Centrifugal Pump, *Applied Sciences* 11, 8180.

Yang, Y., L. Zhou, W. Shi, Z. He, Y. Han and Y. Xiao (2021). Interstage difference of pressure pulsation in a three-stage electrical submersible pump. *Journal of Petroleum Science and Engineering* 196, 107653.

Ye, W., Z. Qian, R. Huang, X. Li, Z. Zhu and X. Luo (2020). Instability analysis for a centrifugal pump with straight inlet pipe using partially averaged Navier–Stokes model, *Proceedings of the Institution of Mechanical Engineers, Part A: Journal of Power and Energy*, 0957650920919540.

Zhang, N., B. Gao, B. Xia and Q. F. Jiang (2020). Effect of the volute tongue cut on pressure pulsations of a low specific speed centrifugal pump, *Journal of Hydrodynamics* 32, 758-70.

Zhang, N., X. Liu, B. Gao, X. Wang and B. Xia (2019). Effects of modifying the blade trailing edge profile on unsteady pressure pulsations and flow structures in a centrifugal pump, *International Journal of Heat and Fluid Flow*, 75, 227-38.

Zhu, B., H. X. Chen, Q. Wei and R. Zhang (2012). "The analysis of unsteady characteristics in the

low specific speed centrifugal pump with drainage gaps." In *IOP Conference Series: Earth and Environmental Science*, 032049. IOP Publishing.

Zhu, Z., X. Jia, J. Yu, B. Li and L. Zhang (2022). Effect of Incident Angle of Wear-ring Clearance on Pressure Pulsation and Vibration Performance of Centrifugal Pump. *Frontiers in Energy Research*, 250.

Zore, K., B. Sasanapuri, G. Parkhi and A. Varghese (2019). August. Ansys mosaic poly-hexcore mesh for high-lift aircraft configuration. In *21st AeSI Annual CFD Symposium*.

Zore, K., D. Caridi and I. Lockley (2020). Fast and accurate prediction of vehicle aerodynamics using ANSYS mosaic mesh (No. 2020-01-5011). *SAE Technical Paper*.